Wild-type GBA1 increases the α-synuclein tetramer–monomer ratio, reduces lipid-rich aggregates, and attenuates motor and cognitive deficits in mice

Kelly E. Glajch[a], Tim E. Moors[b], Yi Chen[a], Pascal A. Bechade[b], Alice Y. Nam[b], Molly M. Rajsombath[b], Thomas D. McCaffery[b], Ulf Dettmer[b], Andreas Weihofen[a], Warren D. Hirst[a], Dennis J. Selkoe[b,1], and Silke Nuber[b,1]

[a]Neurodegenerative Diseases Research Unit, Biogen, Cambridge, MA 02142; and [b]Ann Romney Center for Neurologic Diseases, Department of Neurology, Brigham and Women's Hospital, Harvard Medical School, Boston, MA 02115

Edited by Anders Björklund, Lund University, Lund, Sweden, and approved June 11, 2021 (received for review February 19, 2021)

Loss-of-function mutations in acid beta-glucosidase 1 (GBA1) are among the strongest genetic risk factors for Lewy body disorders such as Parkinson's disease (PD) and Lewy body dementia (DLB). Altered lipid metabolism in PD patient–derived neurons, carrying either GBA1 or PD αS mutations, can shift the physiological α-synuclein (αS) tetramer–monomer (T:M) equilibrium toward aggregation-prone monomers. A resultant increase in pSer129+ αS monomers provides a likely building block for αS aggregates. 3K αS mice, representing a neuropathological amplification of the E46K PD–causing mutation, have decreased αS T:M ratios and vesicle-rich αS+ aggregates in neurons, accompanied by a striking PD-like motor syndrome. We asked whether enhancing glucocerebrosidase (GCase) expression could benefit αS dyshomeostasis by delivering an adeno-associated virus (AAV)–human wild-type (wt) GBA1 vector into the brains of 3K neonates. Intracerebroventricular AAV-wtGBA1 at postnatal day 1 resulted in prominent forebrain neuronal GCase expression, sustained through 6 mo. GBA1 attenuated behavioral deficits both in working memory and fine motor performance tasks. Furthermore, wtGBA1 increased αS solubility and the T:M ratio in both 3K-GBA mice and control littermates and reduced pS129+ and lipid-rich aggregates in 3K-GBA. We observed GCase distribution in more finely dispersed lysosomes, in which there was increased GCase activity, lysosomal cathepsin D and B maturation, decreased perilipin-stabilized lipid droplets, and a normalized TFEB translocation to the nucleus, all indicative of improved lysosomal function and lipid turnover. Therefore, a prolonged increase of the αS T:M ratio by elevating GCase activity reduced the lipid- and vesicle-rich aggregates and ameliorated PD-like phenotypes in mice, further supporting lipid modulating therapies in PD.

α-synuclein | tetramer | glucosylcerebrosidase | cathepsin | GBA

GBA1 gene mutations in Gaucher's disease carriers are recognized as the most important risk factors for developing Parkinson's disease (PD), since large multicenter patient cohorts identified GBA variants in PD, including in ∼3% of sporadic PD patients and up to ∼15% of the Ashkenazi Jewish population with PD (1). Homozygous and heterozygous GBA1 mutation carriers display a similar risk (∼20%) of developing PD (2). GBA1 mutations can impact the activity of its gene product, the lysosomal lipid metabolism enzyme glucocerebrosidase (GCase), leading to changes in cellular lipid content and lipid membrane morphologies (3, 4). Clinically, PD patients with GBA1 mutations are largely indistinguishable from the idiopathic form. Both populations exhibit widespread α-synuclein (αS)+ Lewy bodies (LBs), including in the hippocampus and other brain regions, and these are associated with motor deficits and cognitive decline (2). PD-GBA1 mutation carriers are at a greater risk of cognitive impairments, and this finding is consistent with a higher incidence of GBA1 mutations in =DLB patients (5, 6). Recent morphological analyses of "sporadic" PD brain tissues have revealed that Lewy-type inclusions also contain substantial amounts of lipid-rich membranes and vesicles, including lysosomes (7). Additional evidence for the role of GCase in αS homeostasis has been generated in mouse studies and in GBA1-mutant neural cells, suggesting increased accumulation of αS secondary to different pathogenic GBA1 mutations (8–11).

Accumulating evidence from our laboratory (12–14) and others (15–18) shows that αS normally occurs in a dynamic equilibrium between helically folded tetramers and "natively unfolded" monomers. Regarding the relevance of αS tetramers to disease, we found that all familial PD (fPD)–causing αS mutations decrease the physiological tetramer–monomer (T:M) ratio and some induce cytoplasmic inclusions and neurotoxicity in human (hu) and rodent cell culture (13). Supporting these findings, neurons harboring PD-causing GBA1 mutations shifted endogenous wild-type (wt) αS tetramers to monomers that lead to abnormal phosphorylated serine 129 αS (pS129) + αS accumulation (18), indicating lipid metabolism can impact physiological αS homeostasis. Mechanistic studies have shown that saturated fatty acids (SFAs) stabilize normal tetramers, while unsaturated FAs, such as oleic acid, decrease the T:M ratio (19, 20). Accordingly, decreasing stearoyl-CoA desaturase

Significance

The mechanisms responsible for brain α-synuclein (αS) dyshomeostasis, caused by Gaucher's GBA1 mutations that increase Parkinson's disease (PD) risk, are largely unknown. We previously showed that abrogating physiological αS tetramers by a familial PD-E46K–amplified 3K mutation produces PD-like syndrome in mice and that treatment with stearoyl-CoA desaturase inhibitors increased a portion of the αS tetramers, benefitting the motor phenotypes. Here, we show that—similar to previous findings in GBA1-mutant PD culture—GCase elevation prolonged the stabilization of wild-type and 3K mutant αS tetramers in wtGBA1–transduced mouse brains, improving lysosomal integrity and motor and cognitive phenotypes. These data help elucidating lipid modulators that impact the αS physiological state in vivo and the development of PD therapeutic approaches.

Author contributions: K.E.G., T.E.M., and S.N. designed research; K.E.G., T.E.M., Y.C., P.A.B., A.Y.N., M.M.R., T.D.M., and S.N. performed research; K.E.G., T.E.M., Y.C., P.A.B., A.Y.N., M.M.R., T.D.M., and S.N. analyzed data; and K.E.G., T.E.M., P.A.B., U.D., A.W., W.D.H., D.J.S., and S.N. wrote the paper.

Competing interest statement: D.J.S. is a director and consultant of Prothena. K.E.G., Y.C., A.W., and W.D.H. are employees of Biogen.

This article is a PNAS Direct Submission.

This open access article is distributed under Creative Commons Attribution-NonCommercial-NoDerivatives License 4.0 (CC BY-NC-ND).

[1]To whom correspondence may be addressed. Email: snuber@bwh.harvard.edu or dselkoe@bwh.harvard.edu.

This article contains supporting information online at https://www.pnas.org/lookup/suppl/doi:10.1073/pnas.2103425118/-/DCSupplemental.

Published July 29, 2021.

(SCD) activity, the rate-limiting enzyme for generating monounsaturated (MU) FA, decreases αS+ neuronal inclusions in yeast, rat cortical neurons, hu wt, fPD E46K–induced neurons, and in 3K cell culture models (19–21).

Our recent approach to treating hu wt or 3K αS mutant mice with SCD inhibitors showed that the prolonged increases in the T:M ratio can reduce excess triacylglycerides (TAGs), lipid droplets (LDs) (rich in TAGs), and pS129 αS+ aggregates, aiding multiple PD motor phenotypes (22). Intriguingly, overexpressing hu wtGBA increased the αS T:M ratio in Gaucher's GBA1-mutant neuronal culture (18).

Whether early transduction and prolonged increase of hu wtGCase can enhance αS T:M homeostasis in vivo has yet not been examined. To begin investigating this question, we used the tetramer-abrogating "3K" αS mutant mouse line that is a biochemical amplification of the E46K mutation-causing PD. The 3K mutation shifts the normally aggregation-resistant αS tetramers (12) to increased levels of monomers that then cluster with vesicle membranes and form sizeable aggregates, thereby producing multiple PD-like motor phenotypes by the age of 6 mo (23). The Thy1.2 promotor that drives the 3K transgene reaches stable expression from postnatal day 7 onwards (24), thereby enabling us to study whether GBA1 effects the onset of αS dyshomeostasis in mouse brain when injecting it into 3K neonates. Here, we transduced an adeno-associated virus (AAV)–wtGBA1 vector by intracerebroventricular (ICV) injections in 3K and control littermate pups at P1 and then, 6 mo later, performed motor and cognitive testing and examined the brains for αS species, GCase activity, lysosomal abnormalities, and lipid aggregation patterns.

Results

Regional and Cellular Distribution of hu GCase after Neonatal wtGBA1 Transduction. We first characterized the hu wtGCase expression pattern produced by ICV injections of P1 neonates, as indicated

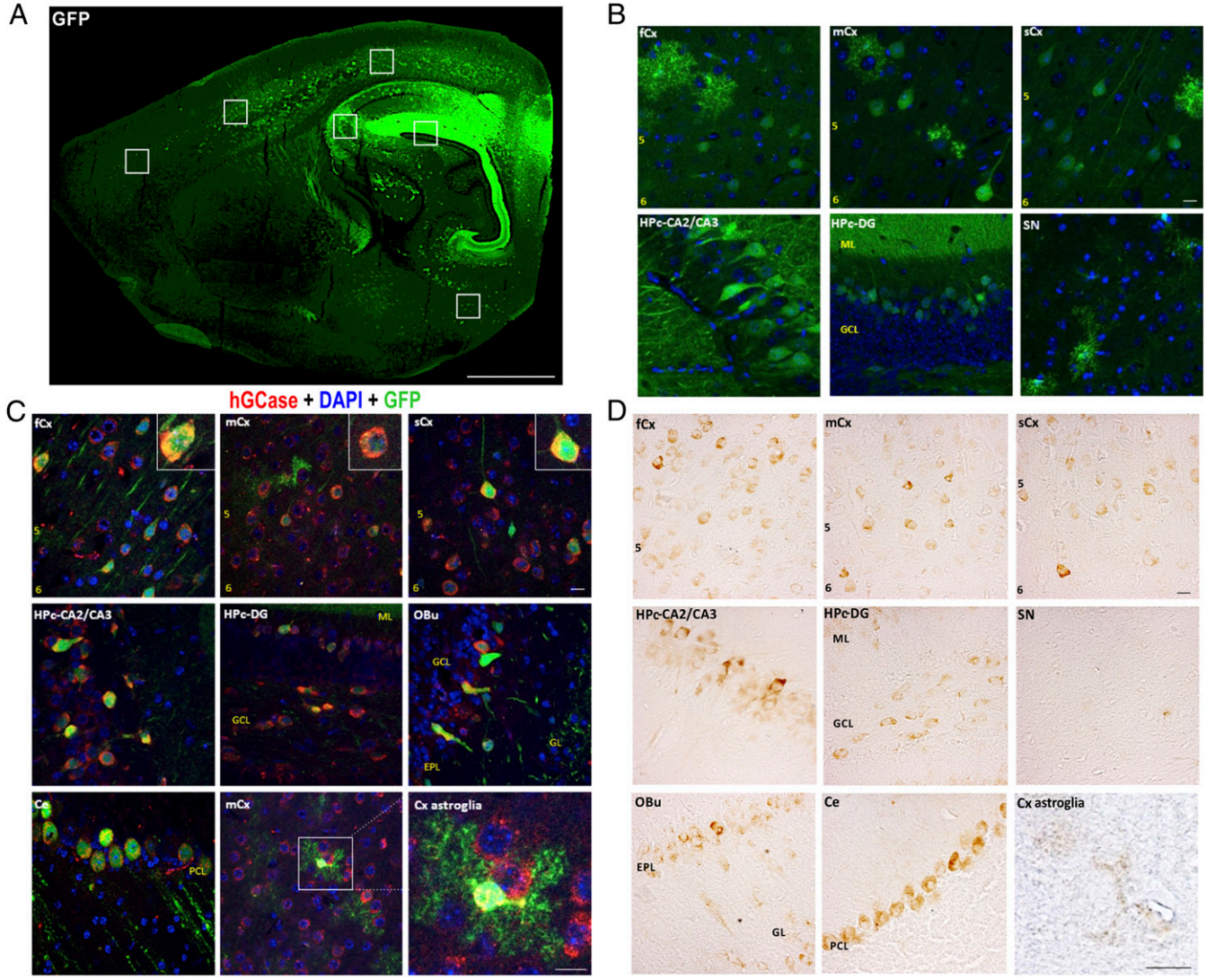

Fig. 1. Neonatal AAV–hu GBA1 delivery induces pronounced expression in the forebrain neurons. P0/P1 3K mice and Ntg littermates were directly injected into the cerebral lateral ventricles with either AAV-vector-p2A-GFP or AAV–hu GBA1-p2A-GFP. Tissues were collected 6-mo postinduction. (*A*) Representative sagittal section showed GFP expression in a hu GBA1-injected mouse. (*B*) Magnification of insets in *A* showed the prominent staining of neurons and occasionally protoplasmic astroglia. (*C*) Staining with a monoclonal ab specific against hu GBA substantiates colocalization with GFP+ cells. (*D*) Staining against hu GBA and visualizing with DAB by light microscopy, validated subregional expression pattern seen with fluorescence staining. fCx, frontal cortex; mCx, motor cortex; sCx, somatosensory cortex; Hpc, hippocampus; DG, dentate gyrus, ML, molecular layer; GCL, granular cell layer; EPL, external plexiform layer; PCL, pyramidal cell layer, and SN, substantia nigra. (Scale bars, 25 μm.)

by coexpressed GFP (Fig. 1). The strongest GFP intensities were observed in the forebrain (hippocampus and cortex), with more modest signals in the subcortical regions, including the striatum, thalamus, and midbrain (Fig.1*A*). This regional pattern was in accord with ICV administration of the AAV vector. Under higher magnification, we observed large numbers of GFP-expressing neurons throughout the hippocampal and cortical layers and some sparsely scattered glial cells (Fig. 1*B* and *SI Appendix*, Fig. S1). Costaining with glial markers showed S100β+ cells with a bushy appearance, thus identifying protoplasmic astrocytes, but we did not observe the microglial markers Iba1 or TMEM119 to colocalize with GFP (*SI Appendix*, Fig. S1). Therefore, hu AAV–GCase is likely not expressed in microglia. GFP labeling was mainly found in neurons of the CA2/CA3 subregion of the hippocampus (*SI Appendix*, Fig. S2). Brain regions more distal to the injection site, such as the substantia nigra that only had occasional scattered GFP+ neurons or glia, far fewer than in cortex and hippocampus. Confocal imaging using an antibody (ab) to hu GCase (ab55080; Abcam) showed the expected coexpression pattern with GFP (Fig. 1*C*) in the cortical and hippocampal layers, and this pattern was further substantiated by light microscopic analyses of hu GCase in 3,3′-diaminobenzidin (DAB)–stained, adjacent sagittal sections (Fig. 1*D*). Based on these data, we conclude that GBA1 was transduced mainly in neurons and was predominantly expressed in the cortex and hippocampus but also in a small number of cells in regions distant from the lateral ventricle, presumably because of viral particles that diffused through the brain.

Transduction with hu wtGBA1 Improves Both Cognitive and Motor Deficits of 3K PD Mice. Given the high expression of wtGCase in hippocampus and cortex, we assessed cognitive changes in hu GBA– and vector-injected littermates at the age of ∼6 mo in a Y-Maze, widely used for testing hippocampus-dependent spatial working memory (Fig. 2). The results revealed that 3K vector (3K-vec) mice displayed a significant deficit in spatial working memory, evidenced by a decrease in alternation of the three Y-Maze arms, as qualitatively depicted by superimposed images of all mouse tracks (Fig. 2*A*, yellow, highlighting an overlay of mouse tracks) and quantified via automated tracking analyses (Fig. 2 *B*–*D*). Two-way ANOVA confirmed that expressing wtGBA1 increased the spontaneous alternation of 3K mice [interaction: $F_{(1,38)} = 7.9$; $P < 0.01$; GBA1 expression: $F_{(1,38)} = 3.9$; $P = 0.05$] toward the performance levels of healthy vector or GBA-transduced nontransgenic (Ntg) littermate mice (Fig. 2*B*). The test further revealed a decreased latency of 3K-vec mice to enter the new (blocked) arm ($P < 0.05$) (Fig. 2*C*), and this was improved in 3K-GBA mice. To exclude the possibility that the observed defects in spatial working memory were due to a decrease in locomotor activity in 3K-vec, we evaluated ambulatory activity by measuring the covered distance in the Y-Maze over the testing period and found no differences between the groups (Fig. 2*D*). To further explore motor skills, we placed mice on a pole and measured the time to climb down the pole (Fig. 2*E*). 3K-GBA mice showed a notable decrease in time required to climb down, becoming similar to control littermates [GBA treatment $F_{(1,38)} = 6.68$; $P = 0.013$].

wtGBA1 Improves Soluble αS Tetramer–Monomer Homeostasis in 3K Mice. Our previous studies established that the E46K-related 3K mutation shifted the normal αS T:M ratio toward excess aggregation-prone monomers, and this led to biochemical changes and PD-like neuropathology (23). AAV-wtGBA1 injection into 3K neonates allowed us to explore wtGBA1 effects very close to the onset of 3K αS expression, given that the AAV vector (25) and the Thy1 promoter of the transgene (24) can each induce stable expression within 7 to 10 d after birth. We first quantified hu and total (t = rodent + hu) GCase (tGCase) to estimate the induced enzyme expression level in cortical brain extracts (Fig. 3). We found that GBA1-transduced mice robustly expressed hu GCase (*SI Appendix*, Fig. S3*A*), and this elevated the total amount of GCase (Fig. 3 *A* and *B*). Since the level of the GCase enzyme correlates with its activity (26), the results suggested an increase in GCase activity (that we also validated by an activity assay; see Fig. 5C). Immunoblotting with the hu αS–specific ab (Fig. 3*A*) or a mouse + hu ab showed that wtGBA1-transduced mice had increased Tris-buffered saline (TBS)–soluble αS and lessened radioimmunoprecipitation assay (RIPA)–soluble αS versus empty vector–treated mice (Fig. 3*C*).

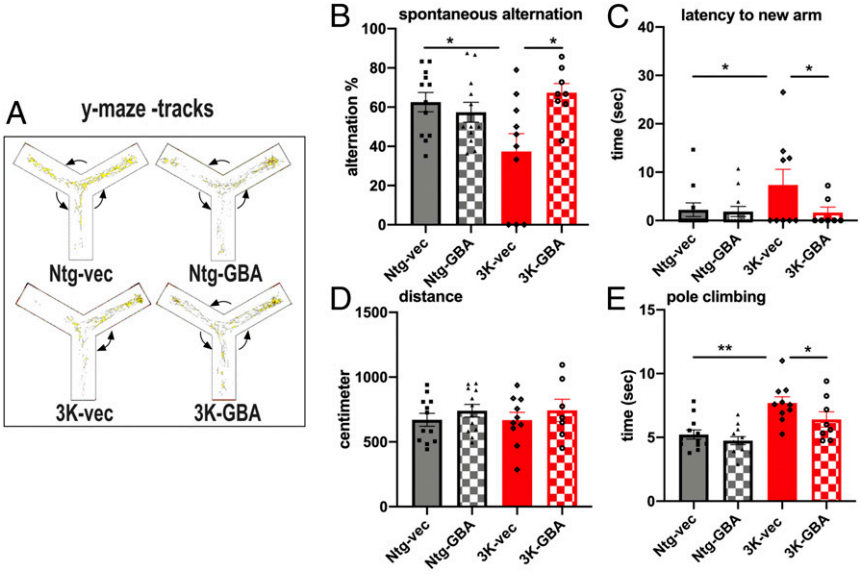

Fig. 2. Induced hu GCase expression "rescues" hippocampal-dependent cognitive function and fine motor skills. GBA1- or vector-transduced 3K and control littermates were subjected to the Y-maze at age 6 mo. (*A*) Digital mouse tracks were summed to generate one superimposed image, a heat map of tracks generated using the FIJI plugin "LUT smart," and exported as a 16-bit image. Spontaneous alternation (*B*), latency (*C*), and distance covered (*D*) were recorded as an index for spatial memory and statistically analyzed using Noldus automatic tracking camera and software. (*E*) 3K fine motor abnormalities were tested using the pole climbing test. Data are means ± SEM. $n = 8$ to 12 per group; $^*P < 0.05$ and $^{**}P < 0.01$; two-way ANOVA and Tukey's post hoc test.

Two-way ANOVA confirmed a highly significant treatment effect [$F_{(1,16)} = 24.20$; $P < 0.001$] and genotype effect [$F_{(1,16)} = 26.55$; $P < 0.001$]. In order to assess the impact of wtGCase on the T:M ratio in the 3K mice, we performed intact cell cross-linking using DSG on washed cortical brain bits (13). 3K-GBA mice showed a marked increase in αS tetramers (Fig. 3 *D* and *E*) and a rise in the T:M ratio (Fig. 3*F*), compared to 3K-vec. In vector- and GBA-transduced control (Ntg littermate) mice, the enhanced GCase in the later also raised the αS tetramer level (Fig. 3*E*) and T:M ratio (Fig. 3*F*). Two-way ANOVA confirmed significant treatment ($P < 0.001$) and genotype ($P < 0.001$) effects. We previously observed a relative decrease of the αS T:M ratio in male versus female 3K mice (26). Thus, we analyzed both sexes in the 3K. The three-way ANOVA (sex × genotype × GBA1 treatment) confirmed that the increase in GCase raised the αS T:M ratio to a similar level in male and female 3K mice (*SI Appendix*, Fig. S3).

Since RIPA extracts may also include a portion of dissolved αS deposits that we observed to develop into sizeable vesicle- and lipid-rich inclusions between the age of 3 to 6 mo in 3K versus wt control mice (23), we performed immunohistochemistry using an ab highly specific for pS129 [EP1536Y (27)]. Because αS can also acquire proteinase K-digestion resistance (PK^{res}) when aggregated into Lewy-type lesions that may include lipid membranes (7), brain sections were PK digested and then stained against an aggregate-sensitive pS129 ab (Fig. 3*G*). The PK^{res} aggregates were imaged and quantified with higher-resolution light microscopy (Fig. 3*H*). In GBA-transduced 3K mice, PK^{res} granules were

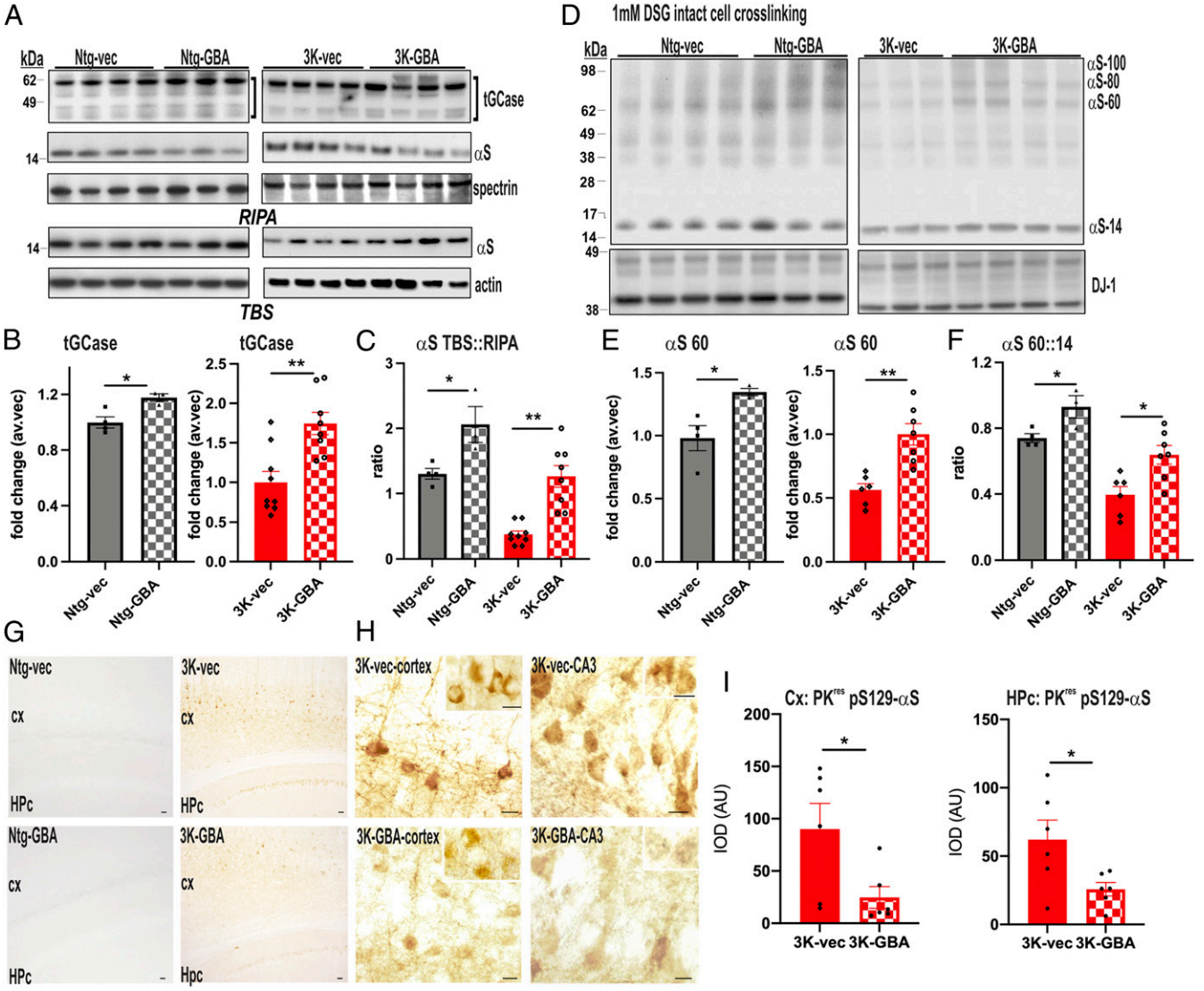

Fig. 3. wtGBA1 increases GCase level, αS solubility, and T:M ratio versus pS129 + aggregate formation in 3K mice. (*A*) WB of hu GCase (hGCase), hu + mouse (total, t) GCase, and hu αS in wtGBA1-transduced 3K and empty vector controls shown in RIPA fraction (*Upper*) and the TBS fraction (*Lower*). β-actin served as the loading control and normalization of relative expression level. Quantification of tGCase (*B*) and αS TBS:RIPA ratio (*C*) by WB. (*D*) Intact cell cross-linking of αS using the cell-penetrant cross-linker DSG in cortical brain bits lysed in PBS/1% Triton X-100. Quantification of the relative tetramer (60 kDa) expression level (*E*) and the αS tetramer to monomer (14 kDa) ratio (*F*) of corresponding WB in *E*. Because blots run at different time points, the empty vector– and GBA-treated 3K and control littermate samples were assessed by unpaired, two-tailed *t* tests. Global GBA1 treatment effects were assessed on the relative αS TBS:RIPA and T:M ratios by two-way ANOVA. (*G, H*) Representative images of PK^{res} pS129+ aggregates in cortex and hippocampus of vector- and GBA-treated 3K and quantitation in *I*. Note that no immunoreactivity was seen in Ntg mice, independent of treatment. Given this unequal distribution of variances between groups, unpaired, two-tailed *t* tests were used to analyze the treatment effect in 3K. IOD, integrated optic density. Data expressed as means ± SEM; $*P < 0.05$ and $**P < 0.01$.

markedly decreased in cortical and hippocampal pyramidal neurons (Fig. 3*J*). Only minimal background immunoreactivity was observed in vector- or GBA1-transduced Ntg control littermates (Fig. 3*G*, *Left*). These findings suggest that a chronic increase in GCase level by AAV-wtGBA1 neonatal transduction preserved a portion of membrane-associated αS monomers from developing into pS129+- and lipid-rich inclusions in 3K mouse brain.

wtGBA1 Reduces Lipid-Rich αS Aggregates and Increases Nuclear TFEB Translocation in 3K Mice. Abnormal, lipidic aggregates are found in hu PD brain (7), in PD-GBA1 mutant neurons (28), and were recently described in a PD fly model (29). We consistently observed pS129 coaggregated with the lysosomal membrane–associated protein1 (LAMP1) in 3K αS mice. The mice develop vesicle-rich inclusions containing multilaminar membranes (26) and Lewy body–type aggregates (23), and these can be decreased by down-regulating LD contents via SCD inhibition (30). Nile Red (NileR) is an established histochemical marker for neutral lipids and LDs (31, 32). Therefore, we quantified NileR+ puncta colocalizing with pS129+ αS aggregates in 3K brain hippocampal neurons (Fig. 4 *A* and *B*, graph). wtGBA1 decreased the NileR+ puncta in 3K neurons ($P < 0.01$). In order to assess whether these changes were the general effects of GBA1, we included the GBA-transduced control littermates in the analyses. Two-way ANOVA revealed a significant interaction [$F_{(1,20)} = 16$; $P < 0.001$] and post hoc paired comparison showed that the excess NileR+ positive foci were decreased in the 3K-wtGBA1 versus 3K-vec mice ($P < 0.01$) and became more similar to the (unchanged) NileR+ puncta detected in Ntg mice. Additionally, Plin2, a coat protein whose binding shields LDs from cytosolic degradation, if not being stripped off by lysosomal

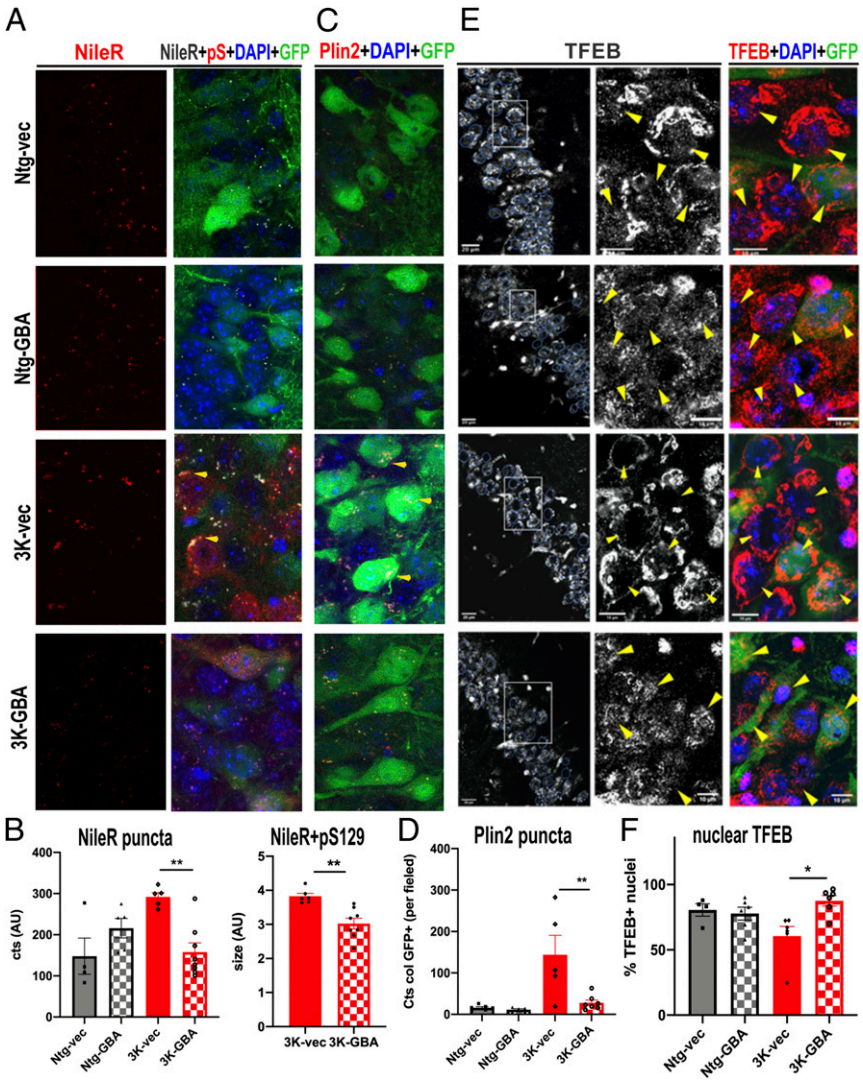

Fig. 4. wtGBA1 decreases lipid-rich pS129+ αS aggregates and increases the nuclear translocation of TFEB in 3K mouse brain. (*A*) Confocal microscopy of hippocampal (hc) sections triple labeled with NileR(gray), pS129 (pS) (red), and DAPI (blue), expressed in GFP+ (green) positive neurons. (*B*) Quantification of NileR puncta in vector- and GBA1-transduced 3K, and Ntg littermates showing a decrease in 3K-vec versus 3K-GBA1 (*Left*) and decrease in lipidic pS129+aggregates (*Right*). (*C*) Plin2 staining identifies excess LDs accumulating in 3K and are reduced in 3K-GBA1–transduced neurons. (*D*) Quantification of LD counts. wtGBA1 increased nuclear TFEB immunoreactivity in 3K hc neurons. (*E*) Representative overview (large image) and magnifications (*Insets*) in the hc CA3 neurons of 3K-vec (*Left*) and 3K-GBA1 (*Right*) mice. Blue circles represent the outline of DAPI-labeled nuclei. Arrowheads (yellow) in the insets highlight nuclear TFEB labeling (red) in 3K-GBA1 mice versus 3K-vec mice. (*F*) Counts of the proportion of hc CA3/CA2 neurons displaying nuclear TFEB immunolabeling. Colocalized points of the respective dual-color confocal images were analyzed for their cts or sizes by using the ImageJ particle analyzer plugin. For spectrally unmixed pS129 and Plin2 staining, see *SI Appendix*, Fig. S4. The quantification of $n = 7$ to 10 fields of three hc sections from each genotype were averaged per mouse ($n = 4$ to 8 each cohort). Data expressed as means ± SEM; $^*P < 0.05$ and $^{**}P < 0.01$; two-way ANOVA, Tukey's post hoc test, or unpaired two-tailed *t* test.

proteases (33, 34), formed numerous immunoreactive foci in 3K-vec mouse brains. This suggests a decrease in lysosomal lipophagy in 3K brain, as we previously observed (22). The excess Plin2-stabilized LDs were decreased in 3K-GBA1 versus 3K-vec mice (Fig. 4 *C* and *D*) (two-way ANOVA interaction: $P = 0.0067$), indicating increased lysosomal lipid turnover following higher GCase activity in 3K mouse brain. Previous studies showed that a high-lipid load retains the transcription factor EB (TFEB) in the cytosol (35). Nuclear TFEB induces genes involved in autophagy and lysosomal biogenesis, thereby contributing to the degradation of cytoplasmic, lipidic material (35–37). We investigated whether the reduction of hippocampal, lipidic pS129+ aggregates in wtGBA1-transduced 3K mice could associate with increased nuclear TFEB immunoreactivity in CA2/CA3 hippocampal neurons. Confocal analyses of double-labeled sections (TFEB and DAPI) showed a relatively lower number of DAPI+ nuclei with TFEB+ in 3K-vec, and this was increased in 3K-GBA–treated mice (Fig. 4 *E* and *F*). Two-way ANOVA of the cell counts revealed a significant interaction [$F_{(1,18)} = 6.3$, $P = 0.02$] and a rise in percentage nuclear TFEB in 3K-GBA versus 3K-vec ($P = 0.015$), becoming similar to TFEB signals in Ntg controls. We only found an average of ∼6 to 7 GFP+ astrocytes in close proximity to GFP+ neurons in hippocampal fields in the CA1 to CA3 region (*SI Appendix*, Fig. S3); thus, it is unlikely that these few astroglia impacted the overall lipid findings. A more likely interpretation of wtGCase effects on 3K αS aggregates is that the observed, neuronal improvement derives from increased, neuronal GCase activity. Together, our data suggest that the increase in soluble T:M homeostasis because of a reduced αS monomer association with membranes is associated with a decrease of lipidic pS129+ aggregates in 3K brain.

Increased Neuronal wtGCase Activity Improves Lysosomal Function and LD Metabolism. Lipidic material, including LDs, can aggregate within LAMP1+ lysosomes because of changes in lysosomal, proteolytic activity (36). Intriguingly, in our vec-3K mice, the sizeable LAMP1+ foci were essentially devoid of GCase immunoreactivity. Transducing wtGBA1 led to an increase in the colabeling of GCase with the more finely distributed LAMP1+ signals in the 3K hippocampal neurons (Fig. 5 *A* and *B*). Two-way ANOVA revealed significant effects in interaction [$F_{(1,20)} = 4.4$; $P = 0.048$] and genotype [$F_{(1,20)} = 6.2$; $P = 0.02$] and GBA treatment [$F_{(1,20)} = 4.9$; $P = 0.038$]. The post hoc paired comparisons showed a significant rise in LAMP1 + GCase–colocalized puncta in the 3K-GBA versus 3K-vec mice ($P < 0.05$). No significant changes were detected in the injected Ntg control littermates. We next analyzed the catalytic activity of GCase, thus providing validation of intact wtGBA1 expression and a potential association to the normalized colocalization pattern observed in 3K neurons. Using the sensitive fluorogenic 4-methylumbelliferyl b-D-glucopyranoside (4MUG) assay (38), we found an overall increase in GCase enzymatic activity (Fig. 5*C*), and two-way ANOVA confirmed a significant treatment effect in the wtGBA1-transduced mice [$F_{(1,32)} = 11.26$; $P = 0.0021$]. This also confirms that the increase of the tGCase protein level detected by Western blotting (WB) (see Fig. 3*A*) is associated with an increase in GCase activity. Therefore, the normalized distribution of GCase to lysosomes was associated with an increase in GCase activity in 3K mice. We next examined immunoreactivity for cathepsin B (CatB), an enzyme that undergoes maturation to its active form by autocleavage at low pH (39). Interestingly, mature CatB can strip off Plins from the LDs when localized to the lysosomal membrane (34). Of note, decreased CatB immunoreactivity and maturation have been described in induced pluripotent stem cells–derived neurons from GBA1-mutant PD patients (40). Confocal analyses revealed sparse CatB densities in 3K-vec–transduced brains, and these increased in 3K-wtGBA1–transduced brains (Fig. 5 *D* and *E*). We found a significant genotype effect [$F_{(1,20)} = 4.4$; $P = 0.049$], and planned comparisons validated the increase in CatB puncta in neurons of 3K-wtGBA1 mice ($P = 0.018$). No differences were detected in control littermates. An increase in lysosomal CatB can increase CatD processing and maturation in mouse brain (41–43). In order to further assess whether the increase in Cat immunoreactivity relates to lysosomal enzymatic maturation, we examined the processing pattern of CatD and CatB by WB, thereby differentiating between higher molecular weight (HMW) forms (proenzyme precursor) and the mature, active form (lower molecular weight, LMW) arising by cleavage at low pH in intact lysosomes (39). We observed significant increases in the mature (LMW) CatD and CatB forms (Fig. 5*F*). When quantifying the LMW as a function of the HMW form, the ratios were significantly increased in 3K-GBA brains ($P < 0.05$) (Fig. 5*G*) and became more similar to the pattern detected in GBA-treated Ntg littermates (*SI Appendix*, Fig. S5). These results suggest that an increase in wtGCase activity improves lysosomal integrity and thereby lysosomal lipid turnover (see summary diagram, Fig. 6).

Discussion

Here, we show that the prolonged induction of hu wtGBA1 beginning at P1 in 3K PD-like mice improves αS solubility and the T:M ratio, associated with reduced, lipidic αS+ aggregates, and improved cognitive and fine motor coordination at the age of 6 mo. These data provide key in vivo preclinical data supporting the beneficial effects of targeting GCase to improve soluble αS homeostasis in PD. Several of our findings are informative for the future design of such therapies, including the positive effects through 6 mo treatment, even with modest increases of wtGCase (∼15% level and activity), and that prolonged stabilization of αS tetramers was associated with benefits for secondary, PD-like alterations, including lysosomal abnormalities. Moreover, increasing GCase activity also enhanced nonmutant (wt) αS solubility and the T:M ratio of GBA1-transduced control (Ntg) littermate mice. Since GCase deficiency may also occur in some idiopathic PD cases (44, 45), these results suggest that targeting GCase could benefit αS homeostasis beyond αS genetic PD forms.

In previous wtGBA1 overexpression studies using transgenic mouse models of PD, GCase-dependent changes in monomeric αS were not observed (10) or not tested (46), or it was reported that only (Tris-) soluble, monomeric αS decreased (47). In contrast, we used a well-established (48) and validated (13, 18) intact cell cross-linking method to capture all αS forms, including the aggregate-resistant αS tetramers (13), and performed sequential extractions to test for soluble and membrane-associated αS. Overexpressing GCase reduced pathological pS129+ αS deposits that colocalized with the lysosomal membrane and lipidic material. Accordingly, the more dispersed and smaller-sized lysosomal (LAMP1+) and lipid (NileR+ or Plin2+) puncta in GBA1-transduced neurons decrease in the pS129+ vesicle- and lipid-rich aggregates, indicating an improved vesicle flux (9) versus coaggregation into multilamellar and fibrillar aggregates by electron microscopy (23, 26). The observed increase in Plin2+ puncta in untreated 3K mouse brain (22) suggests lysosomal deficiencies (29), since these LD membrane coat proteins are stripped off at acidic pH (33). Overexpressing GCase likely promotes lysosomal, enzymatic activities. CatB can process CatD (43), and a new study reported increasing GCase activity in GBA-mutant cell–promoted CatD processing and activity, and this decreased monomeric αS (49). Consistently, we observed an increase in CatD and CatB maturation (Fig. 5). CatB is a newly reported risk factor for PD penetrance in GBA1-mutant carriers [i.e., displaying reduced CatB maturation in the patient-derived neurons (40)]. Additionally, CatB can degrade Plin-coated LDs (22), suggesting that CatB contributes to neuronal lipolysis. Therefore, one could hypothesize that an excess of Plin-stabilized LDs due to a decrease in CatB activity further retains TFEB in the cytosol (50), as supported by less nuclear staining in the 3K brain, and these together lead to formation of αS aggregates (Fig. 6: "disease"). Thus, increasing GCase and other lysosomal, enzymatic activities in PD or Gaucher

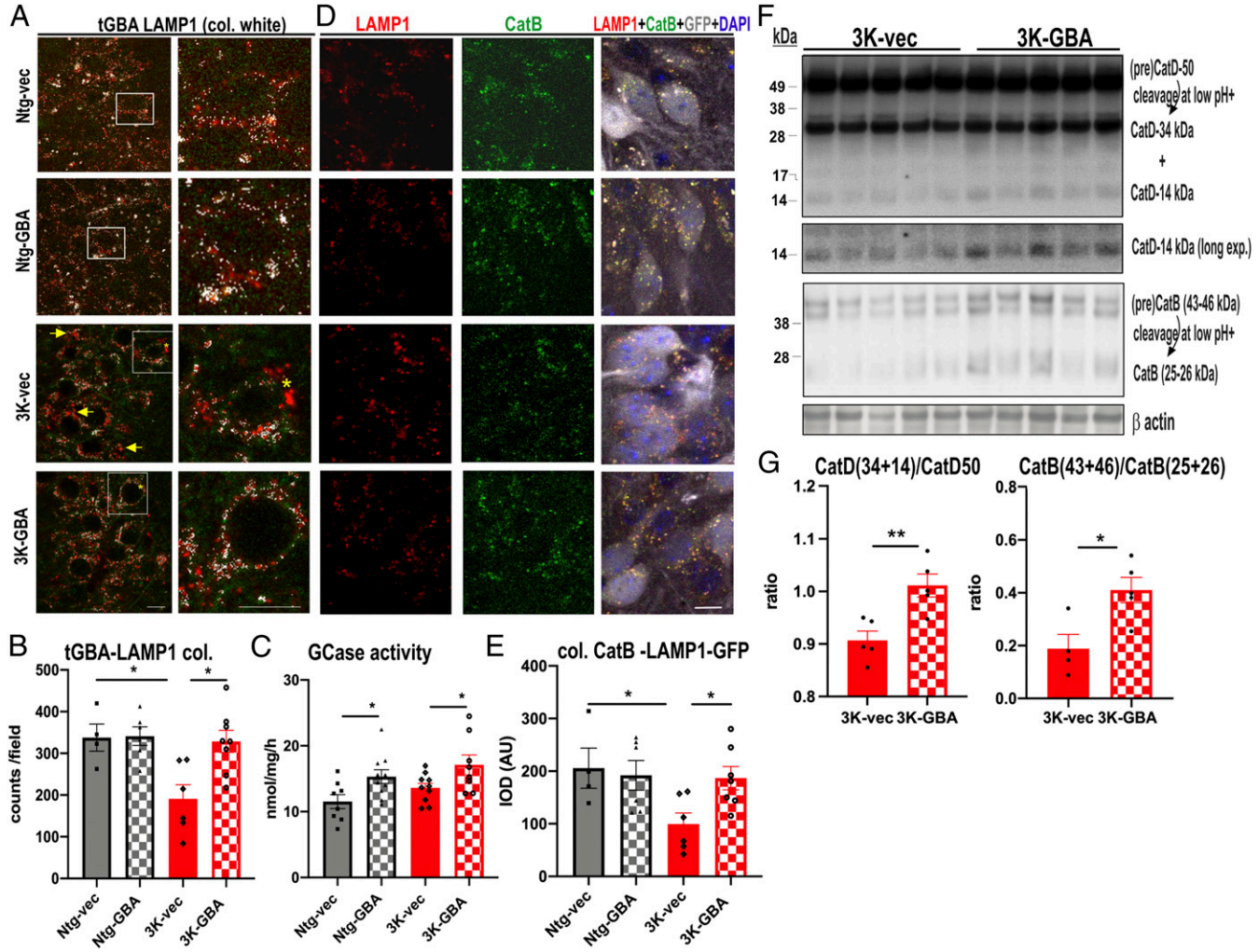

Fig. 5. wtGBA1 increases lysosomal enzyme maturation and activity. The sizeable LAMP1+ foci (FIJI "Maxima" plugin) lacked tGCase reactivity in 3K (magnified on the *Right*), and GBA1 induction increased the colocalization of tGCase with more finely distributed LAMP1 puncta (*A*) and quantitation of colocalized puncta (*B*). (*C*) GCase activity measured in the cortex of GBA or vector-injected 3K and non-Ntg littermates at 6-mo postinjection using the 4MUG assay. Increased CatB immunoreactivity in GBA versus vec-3K (*D*) and quantification (*E*). (*F*) WB shows preforms of CatD (50 kDA) and CatB (43 to 46 kDA) and their LMW (CatD at 14 + 34 kDa and CatB at 25 to 26 kDa) products, representing cleavage at low pH+, consistent with increased CatB immunoreactivity and colocalization with LAMP1+ shown in *D*. (*G*) Quantification of the ratio between the higher and lower molecular signals of CatD and CatB. For histological analyses, $n = 7$ to 10 fields of three hippocampal sections from each genotype ($n = 3$ to 4 each cohort). IOD, integrated optic density; col, colocalization; exp, exposure. Data are expressed as means ± SEM; $*P < 0.05$ and $**P < 0.01$; two-way ANOVA, Tukey's post hoc test, or unpaired two-tailed *t* test. (Scale bars, 20 μm.)

patients may help to normalize lipid homeostasis. (Fig. 6: "health"). In addition, increasing GCase activity by small compounds, such as ambroxol, could be used to continuously reduce pS129+-deposited αS in PD cases (51).

These various observations alone do not explain how increased GCase activity can apparently move excess membrane-bound αS monomers toward the formation of more tetramers but that was also seen in GBA1-mutant neurons of Gaucher's carriers with PD that underwent wtGBA1 transduction (18). Interestingly, GCase preferentially turns over unsaturated glucosylceramides, and this can increase the lipid order of membranes (3). Intriguingly, adding SFA (versus unsaturated FA) to certain PD-relevant cell culture models resolved αS inclusions (19). The apparent increase in relative SFA levels could decrease membrane fluidity, including that of lysosomes, and thereby decrease αS on the membrane (52). Therefore, an increase in GCase activity may promote αS monomer solubility and their subsequent assembly into tetramers. Our and other laboratories' previous studies showed that inhibiting SCD, the key enzyme turning saturated FAs into MU FAs, provided protection against αS-induced neurotoxicity in PD-modeling yeast and neuronal cultures (19–21). In our PD-like mouse model, both the pharmacological inhibition (using the 5b compound) and genetic deletion of SCD1 (SCD knockout [KO] mice or SKO) could stabilize the αS T:M equilibrium. Decreasing SCD activities also decreased excess TAGs, reduced Plin-coated LDs, and improved motor phenotypes at either 3 or 6 mo in 3K-SKO mice (22). Hence, it is likely that certain alterations in the neuronal lipid composition can promote PD pathogenesis by acting on lysosomal lipid clearance pathways. This concept fits with the growing evidence that lipid dyshomeostasis is an imprint factor in hu PD (7, 53–55), as has been observed in PD-relevant neuronal cultures (19, 56–58) and mouse models (22, 59, 60). Therefore, a likely mechanistic explanation for the therapeutic benefits of GBA expression seen here is a shift in FA balance that contributes to proper, amphipathic α-helix in αS that stabilizes tetramer formation, perhaps by enhancing the transient interaction of αS monomers with highly curved vesicle membranes. Additional studies are needed to clarify the relationship between GCase-modified lipid

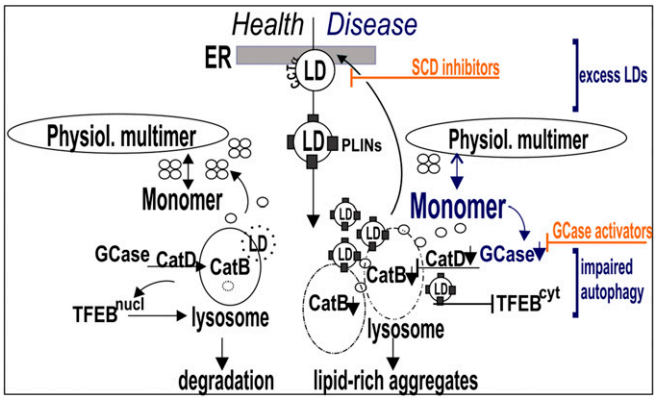

Fig. 6. Hypothetical pathway of shifting native αS multimers toward excess monomers and therapeutic approaches against the buildup of lipid-rich and lysosomal foci. Lysosomal dysfunction—by GCase deficiency or other autophagy perturbations—induced by excess αS monomers at membranes, decreases CatB activity (a risk factor of PD penetrance in hu GBA1 carriers that can strip off perilipins), and this, in turn, yields to Plin-stabilized LDs unavailable for cytosolic degradation. The resultant, nutritional stress stimulates the production of new LDs, and their abnormal membrane expansion is detected by CCT-α [as in Gaucher's Disease neuropathology (66)]. The relative abundance of cytosolic LDs retains TFEB in the cytosol (cyt) versus translocation to the nucleus (nucl), critical for lysosomal biogenesis and thereby lipid degradation (35, 37, 50). The treatment with an SCD inhibitor ("5b") likely acts upstream of this vicious cycle by decreasing unsaturated FAs that are typically stored in form of TAGs, the major component of LDs, thereby reducing the abundance of lipidic material. Alternatively, but not mutually exclusive, a relative increase in SFAs (by SCD inhibitor or increased GCase activity) can produce higher-order lipid domains in membranes and thereby create an αS- (and other protein) repellant surface, increasing the solubility of αS monomers that assemble dynamically into physiological αS tetramers and subsequently decrease the vesicle- and lipid-rich aggregates. Finally, certain SFAs can stabilize the helical structure of αS (67) and thereby the tetramer formation. For additional references of the hypothesized pathway, see *Results* and *Discussion* and our previous publication (22).

metabolism and the αS T:M equilibrium and whether increasing FA saturation (e.g., by SCD inhibition) can increase physiological αS homeostasis in mice with additional mutant GBA1-induced neuropathologies.

Materials and Methods

Experimental Animals and AAV Injection. Recombinant single-stranded AAV.PHPB-CAG-GBA1-p2A-eGFP ("GBA1") and AAV.PHPB-CAG-p2A-eGFP–control empty vector ("vec") were prepared by triple transfection and purified by ion exchange chromatography. To quantify titers, AAV samples were treated with DNase I, diluted, and combined with droplet digital PCR Supermix for probes (no UTP) and a primer/probe mix specific for hu GBA1. Droplets were produced and analyzed using QX200 with the AutoDG system from BioRad. Final titers of the injected solutions were 3.71e13 gc/mL for empty vector and 3.27e12 gc/mL for AAV1-GBA1. A total of 4 μL viral vector and 0.1% (volume/volume) fast green (Sigma) were injected unilaterally. The dye confirmed distribution into both ventricles of each injected P1 neonate.

Sequential Tissue Extractions. Mice were anesthetized, transcardially flushed with cold phosphate-buffered saline (PBS), decapitated, and the brains dissected on a chilled stage. Sequential extractions were performed as described (61). Briefly, small pieces of cortex were homogenized via sonication at 4 °C in two volumes of TBS+ [50 mM Tris·HCl, pH 7.4, 175 mM NaCl; 5 mM EDTA; and protease inhibitor mixture (Calbiochem)]; and spun for 45 min at 120,000 *g*. The pellet was subsequently sonicated in RIPA buffer (TBS+, 1% Nonidet P-40, 0.5% sodium deoxycholate, and 0.1% sodium dodecyl sulfate) and incubated for 15 min, followed by ultracentrifugation for 30 min at 120,000 *g*.

Intact Cell Cross-Linking of Brain Tissue. Dissected cortical brain bits were gently minced with a razor blade, washed, and resuspended in PBS with EDTA-free complete protease inhibitors (Roche Applied Science). Intact cell cross-linking was then conducted, as previously described (23). Briefly, the cell-permeable cross-linker DSG was prepared at 1 mM final concentration in DMSO immediately before use. Samples were incubated with DSG for 30 min at 37 °C with rotation. The reaction was quenched by adding Tris, pH 7.6, at 100 mM final concentration and incubated for 5 min at room temperature (RT) with rotation. After quenching and aspiration of the supernatant, cells were lysed in TBS containing 1% Triton X-100. Proteins were separated from cell debris by ultracentrifugation for 45 min at 120,000 *g*.

4MUG GCase Activity Assay. Tissue samples were homogenized in 10 weight per volume buffer (250 mM sucrose, 10 mM Tris pH = 7.5, 1 mM EDTA, and 0.25% Triton X-100 solution with protease/phosphatase inhibitors) using an Omni Ruptor, sonicated in a water bath, and lysed on ice. Samples were centrifuged at 20,000 *g* for 15 mins at 4 °C, and supernatant was collected and quantified with BCA. To measure GCase activity, 3mM 4MUG (Sigma M3633), an artificial substrate of GCase, was incubated with 10 μg lysates with and without 100 mM conduritol-B-epoxide (EMD Millipore 234599), a GBA antagonist, at 37 °C for 1 h. Reactions were stopped with 1 M Glycine (pH 10.8), and fluorescence was detected with a Biotek synergy microplate reader at 365/445 excitation/emission wavelengths. The tGCase activity (nanomole/milligram/hour) was calculated using known concentrations of a 4-methylumbelliferone (Sigma M1381) standard curve.

Western Blot Analyses. For WB, 8 to 15 μg total protein of sequential extracts were each run on 4 to 12% Bis-Tris gels (Invitrogen) and electroblotted onto nitrocellulose membranes (Millipore). All cross-linked samples were blotted on PVDF membranes for the enhanced retention of proteins. For improved immunodetection of αS (monomers of which are prone to washing off filters (62, 63), the membranes were fixed in 4% paraformaldehyde (PFA) for 10 min. After washing in PBST (PBS with 0.2% Tween 20), membranes were blocked for 1 h at RT in PBS containing 5% bovine serum albumin (BSA). Blots were then incubated with either hu-specific GCase (ab55080, 1:1,000; abcam), hu and rodent–detecting GCase (G4171; 1:1,000; Sigma), hu αS (15G7, 1:1,000; Enzo), CatB (RD Biosciences; 1:1,000), or CatD (MAB 1029; RD Biosciences; 1:1,000). Blots with cross-linked samples were incubated with syn1 (Mc42, 1:2,000, BD biosciences). All abs were diluted in PBS containing 5% BSA overnight. After washing with PBST, membranes were probed with appropriate secondary abs (1:3,000, American Qualex), visualized with enhanced chemiluminescence (PerkinElmer), and analyzed with the VersaDoc gel imaging system. Proteins were normalized to β-actin (A5441, Sigma; 1:5,000), which was used as a loading control. DJ-1 was used as a quality control for cross-linking. Quantification of signal intensities was performed as described (64).

Immunohistochemistry. Anesthetized mice were intracardially perfused with PBS and ice cold 4% (wt/volume) PFA in PBS (pH 7.4). The brain was dissected from the skull and postfixed in 4% PFA for another 48 h at 4 °C. Brains were cut into 25-μm cryotome sections. After treatment with H_20_2 (0.3% in PBS, 30 min) and blocking (10% normal goat serum, 1 h), sections were incubated for 12 h at 4 °C with anti–hu GCase (ab55080, 1:200; abcam) or anti–ro + hu GCase (G4171; 1:1,000; Sigma) in PBS. After washing with PBS, sections were incubated with the respective biotinylated secondary abs (1:200 in PBS; vector; and subsequently transferred into avidin–biotin complex solution (1:500 in PBS; Vectastain Elite Kit, Vector Laboratories) for 1 h and visualized with DAB, as previously described (23). For immunofluorescent experiments, sections were blocked in 10% normal donkey serum and incubated overnight at 4 °C with abs to hu or tGCase (ab55080, 1:100; Abcam), LAMP1 (ab25245, 1:500; Abcam), anti-phosphorylated (pS129) αS (ab51253, 1:4,000; Abcam), goat CatB (RD Biosystems, 1:1,000), CatD (MAB 1029; RD Biosystems, 1:1,000), perilipin 2 (sc390169, Santa Cruz; 1:1,000), and TFEB (A700-070, 1:200; Bethyl Laboratories). This was followed by incubation with the appropriate fluorophore-conjugated secondary abs (1:500 in PBS; Alexa 488, 568, and 647) for 3 h at RT. NileR (ab228553; abcam) was diluted 1:500,000, applied for 15 min, and washed five times for 10 min at the final staining step, prior to embedding with DAPI-containing mounting medium (Vectashield). For confocal imaging of TFEB, a Leica TCS SP8 STED 3× microscope (Leica Microsystems) and LAS X navigator software (Leica) was used. Focus was set based on autofocus on the DAPI channel. Z-stacks of 0.9 μm (z-step size 0.15 μm) were made for each image. Confocal microscopy was conducted with an Axiovert 35 microscope (Zeiss) mounted on an MRC1024 laser-scanning confocal microscope (Bio-Rad), and each image was color balanced. Image analyses were done using Fiji ImageJ Software (NIH). The FIJI plugin "colocalization highlighter" created a mask of overlapped pixels. The number or

sizes or percentage area of the colocalized pixels on the resultant 8-bit images were quantified using the analyze particle function plugin.

Y-Maze Test. Working memory was assessed in the Y-Maze with small modifications (65). Briefly, in order to test for spontaneous alternation performance (SAP) percentage all three arms were accessible for each mouse (each arm 15 × 10 × 10 cm). The percentage SAP was determined by using the equation of total alternations (actual alternations) divided by total number of arm entries −2 (possible alternations) × 100 in a session over 3 min. In order to test for recognition memory, one arm of the maze was blocked off, and the mouse was allowed to explore two arms for 3 min. After a 3 min intertrial period, the mouse was returned to the maze with all arms open, and the mice was monitored for the tendency to spend time in the new arm or the known arms for 3 min. The sequence and number of arm entries were traced automatically by an overhead, contrast-detecting camera and entrance time to the arm, distance covered, and percentage SAP were calculated by Noldus EthoVision XT tracking software. A two-dimensional heatmap of the sum of mouse tracks was generated using FIJI plugin LUT smart and exported as a 16-bit superimposed image.

Pole Climbing. Mice were placed with the head oriented toward the top of a 50-cm vertical threaded metal pole with a diameter of 1 cm. Mice were timed as they descended to the base of the pole, as a way to assess their ability to grasp and maneuver on a pole. The timing began as soon as mice oriented themselves downward. A maximum duration time of 1 min was set to avoid exhaustion. The mice were tested for three consecutive trials (climbing down to the base), and average times to "climb down" were calculated for each mouse.

Experimental Treatment Design, Quantification, and Statistical Analysis. Behavioral testing was conducted in 6-mo-old animals as indicated. Experimental details specific for behavioral testing are included in behavior testing below. Details regarding each statistical test, biological sample size (*n*), and *P* value can be found in the corresponding figure legends and *Results*. All data are represented as mean ± SEM. SEM represents the variance within a group. In all experiments, the genotypes can be found in the corresponding legends. Data were collected and processed side by side in a randomized order for all experiments. Behavioral and histological tests were routinely performed blind to the conditions of the experiments. Unpaired, two-tailed *t* tests were used for comparison between two groups, with $P \leq 0.05$ considered significant. For all comparisons involving multiple variables, ANOVA was performed followed by Tukey's post hoc test for paired comparisons using $P \leq 0.05$ for significance. For all experiments, between 4 to 8 (biochemistry and histology) and 5 to 12 (behavior) mice per experiment were used. Outliers, those mice without any movement (nonperformers) in the arm test in (Fig. 2 *D* and *E*), by robust regression and outlier analysis (ROUT; Q = 1%) or Grubbs (0.1%; $n = 1$ for GCase activity in Fig. 5*C*) were removed from the analysis. Bar graphs show the statistical information (mean ± SEM). All statistical analyses were performed using GraphPad Prism.

Data Availability. All study data are included in the article and/or *SI Appendix*.

ACKNOWLEDGMENTS. We thank Saranna Fanning and other members of the D.J.S. laboratory and of the U.D. laboratory and Xiaoping Hronowski (Biogen) for helpful discussions. R. Brathwaite and G. Dove provided administrative assistance. This work was funded by Grants R01 NS099328 (U.D.), R01 NS083845 (D.J.S.), and R01 NS109510 (S.N.) and a gift of the Women's Brain Initiative (S.N.).

1. E. Sidransky *et al*., Multicenter analysis of glucocerebrosidase mutations in Parkinson's disease. *N. Engl. J. Med.* **361**, 1651–1661 (2009).
2. J. Neumann *et al*., Glucocerebrosidase mutations in clinical and pathologically proven Parkinson's disease. *Brain* **132**, 1783–1794 (2009).
3. H. Akiyama, S. Kobayashi, Y. Hirabayashi, K. Murakami-Murofushi, Cholesterol glucosylation is catalyzed by transglucosylation reaction of β-glucosidase 1. *Biochem. Biophys. Res. Commun.* **441**, 838–843 (2013).
4. H. Akiyama *et al*., Glucocerebrosidases catalyze a transgalactosylation reaction that yields a newly-identified brain sterol metabolite, galactosylated cholesterol. *J. Biol. Chem.* **295**, 5257–5277 (2020).
5. R. N. Alcalay *et al*., Glucocerebrosidase activity in Parkinson's disease with and without GBA mutations. *Brain* **138**, 2648–2658 (2015).
6. G. Liu *et al*.; International Genetics of Parkinson Disease Progression Consortium, Specifically neuropathic Gaucher's mutations accelerate cognitive decline in Parkinson's. *Ann. Neurol.* **80**, 674–685 (2016).
7. S. H. Shahmoradian *et al*., Lewy pathology in Parkinson's disease consists of crowded organelles and lipid membranes. *Nat. Neurosci.* **22**, 1099–1109 (2019).
8. I. Fishbein, Y.-M. Kuo, B. I. Giasson, R. L. Nussbaum, Augmentation of phenotype in a transgenic Parkinson mouse heterozygous for a Gaucher mutation. *Brain* **137**, 3235–3247 (2014).
9. J. R. Mazzulli *et al*., Gaucher disease glucocerebrosidase and α-synuclein form a bidirectional pathogenic loop in synucleinopathies. *Cell* **146**, 37–52 (2011).
10. D. Kim *et al*., D409H GBA1 mutation accelerates the progression of pathology in A53T α-synuclein transgenic mouse model. *Acta Neuropathol. Commun.* **6**, 32 (2018).
11. A. Migdalska-Richards *et al*., The L444P Gba1 mutation enhances alpha-synuclein induced loss of nigral dopaminergic neurons in mice. *Brain* **140**, 2706–2721 (2017).
12. T. Bartels, J. G. Choi, D. J. Selkoe, α-Synuclein occurs physiologically as a helically folded tetramer that resists aggregation. *Nature* **477**, 107–110 (2011).
13. U. Dettmer *et al*., Parkinson-causing α-synuclein missense mutations shift native tetramers to monomers as a mechanism for disease initiation. *Nat. Commun.* **6**, 7314 (2015). Correction in: *Nat. Commun.* **6**, 8008 (2015).
14. E. S. Luth, T. Bartels, U. Dettmer, N. C. Kim, D. J. Selkoe, Purification of α-synuclein from human brain reveals an instability of endogenous multimers as the protein approaches purity. *Biochemistry* **54**, 279–292 (2015).
15. W. Wang *et al*., A soluble α-synuclein construct forms a dynamic tetramer. *Proc. Natl. Acad. Sci. U.S.A.* **108**, 17797–17802 (2011).
16. A. J. Trexler, E. Rhoades, N-Terminal acetylation is critical for forming α-helical oligomer of α-synuclein. *Protein Sci.* **21**, 601–605 (2012).
17. J. Burré, M. Sharma, T. C. Südhof, α-Synuclein assembles into higher-order multimers upon membrane binding to promote SNARE complex formation. *Proc. Natl. Acad. Sci. U.S.A.* **111**, E4274–E4283 (2014).
18. S. Kim *et al*., GBA1 deficiency negatively affects physiological α-synuclein tetramers and related multimers. *Proc. Natl. Acad. Sci. U.S.A.* **115**, 798–803 (2018).
19. T. Imberdis *et al*., Cell models of lipid-rich α-synuclein aggregation validate known modifiers of α-synuclein biology and identify stearoyl-CoA desaturase. *Proc. Natl. Acad. Sci. U.S.A.* **116**, 20760–20769 (2019).
20. S. Fanning *et al*., Lipidomic analysis of α-synuclein neurotoxicity identifies stearoyl CoA desaturase as a target for Parkinson treatment. *Mol. Cell* **73**, 1001–1014.e8 (2019).
21. B. M. Vincent *et al*., Inhibiting stearoyl-CoA desaturase ameliorates α-synuclein cytotoxicity. *Cell Rep.* **25**, 2742–2754.e31 (2018).
22. S. Nuber *et al*., A stearoyl-coenzyme A desaturase inhibitor prevents multiple Parkinson disease phenotypes in alpha-synuclein mice. *Ann. Neurol.* **89**, 74–90 (2021).
23. S. Nuber *et al*., Abrogating native α-synuclein tetramers in mice causes a L-DOPA-responsive motor syndrome closely resembling Parkinson's disease. *Neuron* **100**, 75–90.e5 (2018).
24. A. Lüthi *et al*., Endogenous serine protease inhibitor modulates epileptic activity and hippocampal long-term potentiation. *J. Neurosci.* **17**, 4688–4699 (1997).
25. J.-Y. Kim *et al*., Viral transduction of the neonatal brain delivers controllable genetic mosaicism for visualising and manipulating neuronal circuits in vivo. *Eur. J. Neurosci.* **37**, 1203–1220 (2013).
26. M. M. Rajsombath, A. Y. Nam, M. Ericsson, S. Nuber, Female sex and brain-selective estrogen benefit α-synuclein tetramerization and the PD-like motor syndrome in 3K transgenic mice. *J. Neurosci.* **39**, 7628–7640 (2019).
27. V. Delic *et al*., Sensitivity and specificity of phospho-Ser129 α-synuclein monoclonal antibodies. *J. Comp. Neurol.* **526**, 1978–1990 (2018).
28. D. C. Schöndorf *et al*., iPSC-derived neurons from GBA1-associated Parkinson's disease patients show autophagic defects and impaired calcium homeostasis. *Nat. Commun.* **5**, 4028 (2014).
29. V. Girard *et al*., Spen modulates lipid droplet content in adult Drosophila glial cells and protects against paraquat toxicity. *Sci. Rep.* **10**, 20023 (2020).
30. J. A. Fauerbach *et al*., Supramolecular non-amyloid intermediates in the early stages of α-synuclein aggregation. *Biophys. J.* **102**, 1127–1136 (2012).
31. S. O. Zhang, R. Trimble, F. Guo, H. Y. Mak, Lipid droplets as ubiquitous fat storage organelles in *C. elegans*. *BMC Cell Biol.* **11**, 96 (2010).
32. L. L. Listenberger *et al*., Triglyceride accumulation protects against fatty acid-induced lipotoxicity. *Proc. Natl. Acad. Sci. U.S.A.* **100**, 3077–3082 (2003).
33. C. Sztalryd, D. L. Brasaemle, The perilipin family of lipid droplet proteins: Gatekeepers of intracellular lipolysis. *Biochim. Biophys. Acta Mol. Cell Biol. Lipids* **1862**, 1221–1232 (2017).
34. Y. Mizunoe *et al*., Cathepsin B overexpression induces degradation of perilipin 1 to cause lipid metabolism dysfunction in adipocytes. *Sci. Rep.* **10**, 634 (2020).
35. C. Settembre *et al*., TFEB controls cellular lipid metabolism through a starvation-induced autoregulatory loop. *Nat. Cell Biol.* **15**, 647–658 (2013). Correction in: *Nat. Cell. Biol.* **15**, 1016 (2013).
36. R. Singh *et al*., Autophagy regulates lipid metabolism. *Nature* **458**, 1131–1135 (2009).
37. C. Settembre, A. Ballabio, TFEB regulates autophagy: An integrated coordination of cellular degradation and recycling processes. *Autophagy* **7**, 1379–1381 (2011).
38. S. Patnaik *et al*., Discovery, structure-activity relationship, and biological evaluation of noninhibitory small molecule chaperones of glucocerebrosidase. *J. Med. Chem.* **55**, 5734–5748 (2012).
39. C. Vidoni, C. Follo, M. Savino, M. A. B. Melone, C. Isidoro, The role of cathepsin D in the pathogenesis of human neurodegenerative disorders. *Med. Res. Rev.* **36**, 845–870 (2016).
40. C. Blauwendraat *et al*.; 23andMe Research Team, Genetic modifiers of risk and age at onset in GBA associated Parkinson's disease and Lewy body dementia. *Brain* **143**, 234–248 (2020).

41. J. K. Götzl *et al*., Early lysosomal maturation deficits in microglia triggers enhanced lysosomal activity in other brain cells of progranulin knockout mice. *Mol. Neurodegener.* **13**, 48 (2018).
42. G. Werner *et al*., Loss of TMEM106B potentiates lysosomal and FTLD-like pathology in progranulin-deficient mice. *EMBO Rep.* **21**, e50241 (2020).
43. V. Laurent-Matha, D. Derocq, C. Prébois, N. Katunuma, E. Liaudet-Coopman, Processing of human cathepsin D is independent of its catalytic function and auto-activation: Involvement of cathepsins L and B. *J. Biochem.* **139**, 363–371 (2006).
44. D. Chiasserini *et al*., Selective loss of glucocerebrosidase activity in sporadic Parkinson's disease and dementia with Lewy bodies. *Mol. Neurodegener.* **10**, 15 (2015).
45. T. E. Moors *et al*., Characterization of brain lysosomal activities in GBA-related and sporadic Parkinson's disease and dementia with Lewy bodies. *Mol. Neurobiol.* **56**, 1344–1355 (2019).
46. E. Rockenstein *et al*., Glucocerebrosidase modulates cognitive and motor activities in murine models of Parkinson's disease. *Hum. Mol. Genet.* **25**, 2645–2660 (2016).
47. S. P. Sardi *et al*., Augmenting CNS glucocerebrosidase activity as a therapeutic strategy for parkinsonism and other Gaucher-related synucleinopathies. *Proc. Natl. Acad. Sci. U.S.A.* **110**, 3537–3542 (2013).
48. U. Dettmer, A. J. Newman, E. S. Luth, T. Bartels, D. Selkoe, In vivo cross-linking reveals principally oligomeric forms of α-synuclein and β-synuclein in neurons and non-neural cells. *J. Biol. Chem.* **288**, 6371–6385 (2013).
49. S.-Y. Yang, M. Gegg, D. Chau, A. Schapira, Glucocerebrosidase activity, cathepsin D and monomeric α-synuclein interactions in a stem cell derived neuronal model of a PD associated GBA1 mutation. *Neurobiol. Dis.* **134**, 104620 (2020).
50. T. E. Moors *et al*., Therapeutic potential of autophagy-enhancing agents in Parkinson's disease. *Mol. Neurodegener.* **12**, 11 (2017).
51. A. Migdalska-Richards, L. Daly, E. Bezard, A. H. V. Schapira, Ambroxol effects in glucocerebrosidase and α-synuclein transgenic mice. *Ann. Neurol.* **80**, 766–775 (2016).
52. Y. Shen *et al*., Metabolic activity induces membrane phase separation in endoplasmic reticulum. *Proc. Natl. Acad. Sci. U.S.A.* **114**, 13394–13399 (2017).
53. O. R. Brekk, J. R. Honey, S. Lee, P. J. Hallett, O. Isacson, Cell type-specific lipid storage changes in Parkinson's disease patient brains are recapitulated by experimental glycolipid disturbance. *Proc. Natl. Acad. Sci. U.S.A.* **117**, 27646–27654 (2020).
54. P. L. Wood, S. Tippireddy, J. Feriante, R. L. Woltjer, Augmented frontal cortex diacylglycerol levels in Parkinson's disease and Lewy body disease. *PLoS One* **13**, e0191815 (2018).
55. M. E. Gegg *et al*., Glucocerebrosidase deficiency in substantia nigra of Parkinson disease brains. *Ann. Neurol.* **72**, 455–463 (2012).
56. N. P. Alza, M. A. Conde, P. G. Scodelaro-Bilbao, G. A. Salvador, Neutral lipids as early biomarkers of cellular fate: The case of α-synuclein overexpression. *Cell Death Dis.* **12**, 52 (2021).
57. S. Fanning *et al*., Lipidomic analysis of alpha-synuclein neurotoxicity identifies stearoyl CoA desaturase as a target for Parkinson treatment. *Mol. Cell* **73**, 1001–1014.e8 (2019).
58. H. Xicoy, J. F. Brouwers, O. Kalnytska, B. Wieringa, G. J. M. Martens, Lipid analysis of the 6-hydroxydopamine-treated SH-SY5Y cell model for Parkinson's disease. *Mol. Neurobiol.* **57**, 848–859 (2020).
59. X. Han *et al*., Plin4-dependent lipid droplets hamper neuronal mitophagy in the MPTP/p-induced mouse model of Parkinson's disease. *Front. Neurosci.* **12**, 397 (2018).
60. M. Díaz *et al*., Lipostatic mechanisms preserving cerebellar lipids in MPTP-treated mice: Focus on membrane microdomains and lipid-related gene expression. *Front. Mol. Neurosci.* **12**, 93 (2019).
61. S. Nuber *et al*., A progressive dopaminergic phenotype associated with neurotoxic conversion of α-synuclein in BAC-transgenic rats. *Brain* **136**, 412–432 (2013).
62. A. J. Newman, D. Selkoe, U. Dettmer, A new method for quantitative immunoblotting of endogenous α-synuclein. *PLoS One* **8**, e81314 (2013).
63. B. R. Lee, T. Kamitani, Improved immunodetection of endogenous α-synuclein. *PLoS One* **6**, e23939 (2011).
64. S. Nuber *et al*., Neurodegeneration and motor dysfunction in a conditional model of Parkinson's disease. *J. Neurosci.* **28**, 2471–2484 (2008).
65. E. M. Knight, I. V. Martins, S. Gümüsgöz, S. M. Allan, C. B. Lawrence, High-fat diet-induced memory impairment in triple-transgenic Alzheimer's disease (3xTgAD) mice is independent of changes in amyloid and tau pathology. *Neurobiol. Aging* **35**, 1821–1832 (2014).
66. J. Bodennec, D. Pelled, C. Riebeling, S. Trajkovic, A. H. Futerman, Phosphatidylcholine synthesis is elevated in neuronal models of Gaucher disease due to direct activation of CTP: Phosphocholine cytidylyltransferase by glucosylceramide. *FASEB J.* **16**, 1814–1816 (2002).
67. E. I. O'Leary, Z. Jiang, M.-P. Strub, J. C. Lee, Effects of phosphatidylcholine membrane fluidity on the conformation and aggregation of N-terminally acetylated α-synuclein. *J. Biol. Chem.* **293**, 11195–11205 (2018).